Computational and Structural Biotechnology Journal 27 (2025) 3370–3378

Contents lists available at ScienceDirect

Computational and Structural Biotechnology Journal

journal homepage: www.elsevier.com/locate/csbj

Research article

A molecular dynamics protocol for rapid prediction of EGFR overactivation and its application to the rare mutations S768I, S768N, D761N

Julian Behn [a,b], R.N.V. Krishna Deepak [a,c], Jiancheng Hu [d,e], Hao Fan [a,d,f,g,*]

[a] Bioinformatics Institute (BII), Agency for Science, Technology and Research (A*STAR), Singapore 138671, Singapore
[b] Yong Loo Lin School of Medicine, National University of Singapore, Singapore, Singapore
[c] School of Arts and Sciences, Azim Premji University Bangalore, Bangalore, India
[d] Cancer and Stem Cell Program, Duke-NUS Medical School, 8 College Road, Singapore 169857, Singapore
[e] Division of Cellular and Molecular Research, National Cancer Centre Singapore, 11 Hospital Crescent, Singapore 169610, Singapore
[f] Synthetic Biology Translational Research Program, Yong Loo Lin School of Medicine, National University of Singapore, Singapore 117597, Singapore
[g] Department of Biochemistry, Yong Loo Lin School of Medicine, National University of Singapore, Singapore 117596, Singapore

ARTICLE INFO

Keywords:
Kinase
Epidermal growth factor receptor
Asymmetric dimer
Symmetric dimer
Cancer mutations
Molecular dynamics simulation

ABSTRACT

Hyperactivation caused by mutations in the Epidermal Growth Factor Receptor (EGFR) kinase domain is implicated in various diseases, including cancer. However, the structural mechanisms underlying overactivation in many EGFR mutations remain poorly understood, and exploring these mechanisms through conventional experiments or *in silico* simulations is often labor- and cost-intensive. Here, we establish a Molecular Dynamics (MD) protocol capable of rapidly revealing EGFR mutant modes of action using multiple short simulations. We first simulated wild-type EGFR and the well-studied oncogenic mutations L858R and T790M/L858R under different simulation conditions, to derive a protocol which could recapitulate their experimentally established behavior. We then applied this protocol to three rare EGFR mutations: S768I, S768N, and D761N. Experimental studies have suggested that S768I and D761N are oncogenic, whereas S768N is likely a neutral mutation that does not significantly alter EGFR activity. Our simulation results were consistent with these functional indications and provided the corresponding molecular bases – S768I and S768N affect the orientation and stability of the catalytically important αC-helix, while D761N introduces a new hydrogen bonding network between the αC-helix and activation loop. Collectively, the protocol presented here provides a robust and rapid framework for characterizing EGFR mutation mechanisms and is readily adaptable to novel or uncharacterized variants.

1. Introduction

The Epidermal Growth Factor Receptor (EGFR) is a transmembrane tyrosine kinase receptor of major clinical relevance. Mutations in its intracellular kinase domain are key drivers of cancer, particularly in Non-Small Cell Lung Cancer (NSCLC), the most common type of lung cancer [1]. The frequency of EGFR mutations in NSCLC shows demographic variation, ranging from 10 – 20 % in Caucasians to 40 – 60 % in Southeast Asians [2]. Targeted therapies using tyrosine kinase inhibitors (TKIs) have significantly improved outcomes for patients with EGFR-related cancers [3]. However, resistance, either acquired or intrinsic, remains a major obstacle in EGFR-targeted treatment [4]. A deeper understanding of the structural consequences of oncogenic EGFR mutations is therefore critical for advancing therapeutic strategies.

The intracellular kinase domain of EGFR adopts a conserved bilobal fold, comprising an N-terminal lobe and a C-terminal lobe connected by a short hinge region (Fig. 1a) [5,6]. This domain is highly dynamic, switching between multiple conformational states [7–9]. In its active conformation, the interlobal activation loop extends outward to allow substrate access to the ATP-binding pocket. The αC-helix adopts an inward orientation that supports the formation of the crucial K745 – E762 salt bridge, essential for coordinating the ATP – Mg^{2+} complex [10]. The conserved Asp-Phe-Gly (DFG) motif also adopts a conformation that promotes ATP binding. By contrast, in the Src-like inactive conformation, the activation loop collapses over the ATP-binding site, the αC-helix swings outward, and the K745 – E762 salt bridge is disrupted.

---

[*] Corresponding author at: Bioinformatics Institute (BII), Agency for Science, Technology and Research (A*STAR), Singapore 138671, Singapore.
E-mail addresses: hfan2006@gmail.com, fanh@bii.a-star.edu.sg (H. Fan).

https://doi.org/10.1016/j.csbj.2025.07.046
Received 15 May 2025; Received in revised form 23 July 2025; Accepted 23 July 2025

Another inactive state, the ’DFG-out’ conformation, involves the reorientation of the DFG motif to block ATP binding. While most resolved EGFR crystal structures fall into either the active or Src-like inactive states, molecular simulations have identified additional partially disordered conformations that may regulate EGFR activity [11–14]. In the absence of activating ligands, wild-type EGFR predominantly adopts an inactive conformation, and its dynamics are further modulated by dimerization.

EGFR kinase domains form distinct intracellular dimers that regulate activity. In the asymmetric dimer (Fig. 1b), both monomers adopt the active conformation [15]. One monomer (the activator) allosterically stabilizes the αC-helix of the other (the receiver), promoting activation. This mechanism is critical for ligand-dependent activation of wild-type EGFR. Conversely, the symmetric dimer (Fig. 1c) features both monomers in the Src-like inactive conformation, stabilized by interactions between their C-terminal tails, and is implicated in autoinhibition [16]. Apart from the allosteric effects of dimerization on EGFR activity, mutations in the kinase domain can also modulate EGFR conformation and activity.

Over 500 EGFR missense mutations have been documented in the Catalogue of Somatic Mutations in Cancer (COSMIC) database, many of which affect key structural elements that regulate kinase activity, including the activation loop, the αC-helix, or the DFG motif. Even minor perturbations in these regions can shift the conformational equilibrium between inactive and active states. Structural and computational studies have shown that such mutation-induced conformational shifts can promote ligand-independent signaling and alter the efficacy of tyrosine kinase inhibitors [11,17–21]. The exon 21 mutation L858R, along with exon 19 deletion mutations, is among the most frequent drivers of EGFR-positive NSCLC [22]. Located at the start of the activation loop near the DFG motif, L858R stabilizes the active conformation while destabilizing the inactive one [11,23–25]. Patients with L858R mutations often develop a secondary resistance mutation, T790M, resulting in the double mutation T790M/L858R. Although traditionally described as a ‘gatekeeper’ mutation, T790M likely confers drug resistance by increasing ATP affinity rather than through steric effects [26].

Beyond these well-characterized variants, numerous rare and ultra-rare EGFR mutations exist. Most of these remain uncharacterized, and the structural mechanisms underlying their effects are unknown. Among the few rare mutations that have been studied, S768I in exon 20 (0.6 – 1 % of EGFR-positive NSCLC cases) has been shown to be oncogenic in experimental and clinical studies [19,27,28]. Located at the C-terminal end of the αC-helix and oriented away from the binding pocket, S768I was proposed by Shan et al. (identified as S744I in their study) to promote the active conformation via an allosteric mechanism [11]. Their simulations showed increased stability of the αC-helix and enhanced K745 – E762 salt bridge formation, attributed to tighter hydrophobic packing between the isoleucine residue in the αC-helix and the activation loop. However, their study did not quantify this increased hydrophobic packing. In contrast, an ultra-rare S768N mutation, occurring at the same position, has been reported as functionally neutral [29,30]. Its structural basis remains unclear.

Another αC-helix mutation, D761N (exon 19), has been identified in multiple tumor samples. It is associated with increased EGFR activity and TKI resistance [30–32]. Despite its distal location from the ATP-binding site, it may influence activity through an allosteric mechanism. However, its molecular effects are still unknown.

Molecular Dynamics (MD) simulations offer a powerful means to study the structural impact of EGFR mutations by comparing mutant and wild-type dynamics. Prior studies have employed varying system configurations and protocols, including differences in ATP inclusion, dimerization states, conformational starting points, simulation length, and force field parameters [1,9,11–14,18,24,25,33–40]. To date, no benchmarking study has established optimal MD simulation protocols tailored for EGFR. This variability hinders comparability across studies. Furthermore, most existing simulations are long (on the microsecond scale), requiring extensive time and computational resources, limiting their applicability to broad mutation screens.

To address these gaps, we developed a standardized and efficient MD protocol for evaluating EGFR mutants using structural modeling and multiple short simulations. We benchmarked the protocol using CHARMM and AMBER force fields across wild-type, L858R, and T790M/L858R variants as controls. We then applied the same protocol to three rarer mutations: S768I, S768N, and D761N. Our results were consistent with the known biological behavior and revealed distinct structural mechanisms for each variant. Specifically, we confirmed prior observations of increased αC-helix stability and K745 – E762 salt bridge formation in S768I, and further quantified the enhanced hydrophobic

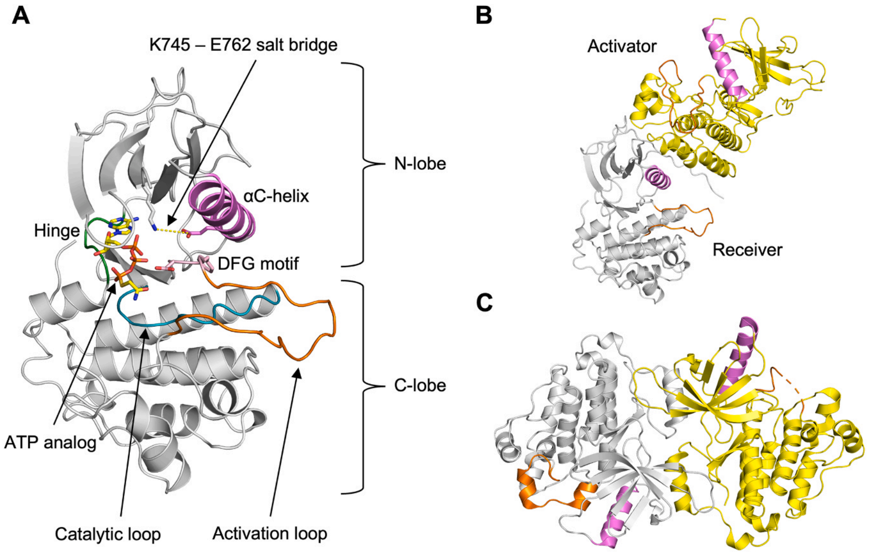

Fig. 1. Structure of EGFR in monomeric and dimeric form. (A) X-ray structure of the EGFR kinase domain in active conformation (PDB: 2GS6), with key structural features highlighted. (B) The kinase domain can form an asymmetric dimer, where both protomers adopt an active-like conformation. The receiver and activator chains are colored gray and yellow, respectively. (C) EGFR can also form a symmetric dimer, in which both chains adopt the Src-like inactive conformation (PDB: 6V66). In this arrangement, the activation loop is collapsed. The chains are colored gray and yellow, respectively. For better comparison, the αC-helices (violet) and activation loops (orange) are highlighted in both (B) and (C).

packing. In contrast, S768N disrupted local hydrogen bonding and exhibited reduced K745 – E762 salt bridge stability, consistent with its neutral phenotype. The D761N mutation, meanwhile, reshaped the hydrogen bonding network, introducing a novel and stable interaction pattern between the αC-helix and the activation loop, offering a new mechanistic insight into its oncogenic potential. Overall, our study presents a rapid and reproducible MD protocol for predicting the oncogenic potential of EGFR mutations and dissecting their molecular mechanisms. Unlike traditional microsecond-scale simulations, our approach yields actionable insights within two days, making it ideal for large-scale EGFR mutation screening.

2. Materials and methods

2.1. Structural modeling

The initial EGFR kinase domain structures were generated using the homology modeling software MODELLER (version 10.4) [41]. For the asymmetric dimer, the active-state crystal structure (PDB:2GS6) was used as the template, while for the symmetric dimer, the inactive-state structure (PDB:6V66) was used. ATP and Mg^{2+} were placed in the ATP-binding pockets of the templates to create ATP-bound models. The canonical EGFR UniProt sequence (AC:P00533), covering residues 697–1022, was used as the wild-type target. Mutations were introduced at the appropriate positions to generate mutant sequences. For each target sequence, 2000 models were generated for both the asymmetric and symmetric ATP-bound dimers. The best model from each set was selected based on the Discrete Optimized Protein Energy (DOPE) score [42]. Model quality was evaluated using MolProbity [43]. Apo (ligand-free) structures were obtained by removing ATP + Mg^{2+} from the selected models.

2.2. Molecular Dynamics (MD) simulations

All simulations were performed with GROMACS (versions 2021.5 and 2022.1) [44], using the CHARMM36m force field [45] or the AMBER ff19SB force field [46]. The input files for the simulations were generated with the CHARMM-GUI web interface (https://www.charmm-gui.org) [47–50]. The N- and C-termini were capped by acetylation and amidation, respectively. All histidine residues were modeled with δ-nitrogen protonation, except H835, which was protonated on the ε-nitrogen. In holo simulations, the ATP molecule was assigned a −4 charge. Each EGFR dimer was placed in a rectangular solvent box with a 10.0 Å buffer from the solute. Na^{+} and Cl^{-} ions were added to neutralize the system and adjust ionic strength to 0.15 M. Energy minimization was performed using the steepest descent algorithm, followed by a 125 ps NVT equilibration at 303.15 K. Production runs were conducted under NPT conditions in five independent 100 ns simulations (‘replicas’) per system, each with randomly initialized velocities, totaling 500 ns per system. Details are provided in Tables S1 and S2 (Supplementary Material).

2.3. Data analysis and visualization

Averaged properties are reported as mean ± standard deviation. Trajectories were analyzed using built-in tools from GROMACS and the Python library MDTraj [51]. The K745 – E762 salt bridge was considered intact when the distance between the NZ atom of lysine and either carboxylate oxygen (OE1 or OE2) of glutamate was $\leq$ 4.0 Å. Activation loop disruption was defined as by a helix pitch $>$ 7.0 Å, measured as the Cα-Cα distance between residues 858 and 862. Protein structures were visualized using the PyMOL Molecular Graphics System, (Version 3.0.2 Schrödinger, LLC).

3. Results

3.1. Benchmarking of the simulation protocol

To develop an effective MD protocol for studying dynamic differences between wild-type and mutant EGFR, we compared two widely used force fields: CHARMM and AMBER. Both the active-like and Src-like inactive conformations were simulated (hereafter referred to as ‘active’ and ‘inactive’) as dimers, with the active state modeled as an asymmetric dimer and the inactive state modeled as a symmetric dimer. To assess the effect of ATP on EGFR dynamics, each dimer was simulated under both apo (ligand-free) and holo (ATP bound in the receiver monomer) conditions. In the symmetric dimer, which lacks a defined receiver chain, ATP was placed arbitrarily in the first chain (chain ‘A’) based on the crystal structure assignment.

For benchmarking, we simulated wild-type (WT) EGFR, the oncogenic L858R mutant, and the drug-resistant double mutant T790M/L858R (henceforth referred to as ‘TMLR’). Each combination of force field, dimer type, state (apo/holo), and EGFR variant (WT or mutant) defined a unique simulation system. Each system was simulated for 500 ns. With 24 systems in total, the benchmarking study amounted to 12 μs of simulation time (Table S1). System stability was assessed by tracking the Root Mean Square Deviation (RMSD) of backbone atoms, which remained stable across all simulations for both force fields (Figures S1 and S2).

3.2. CHARMM vs. AMBER: simulating the asymmetric dimer

A well-established mechanism of EGFR overactivation involves stabilization of the active conformation [11,25]. This conformation is marked by the formation of the catalytically important K745 – E762 salt bridge (Fig. 2a). To evaluate how each force field captures this stabilizing feature, we measured salt bridge occupancy in asymmetric dimer simulations (Fig. 2b).

In CHARMM apo simulations, both mutants showed increased salt bridge occupancy compared to WT in both chains of the asymmetric dimer. In the receiver chain, this effect was particularly pronounced for L858R, which showed an increase of more than 10 percentage points compared to WT (WT: 85.4 %, L858R: 97.1 %, TMLR: 93.8 %). In the apo activator chain, TMLR exhibited a nearly 20 percentage point increase in occupancy, while L858R also showed a substantial increase of over 10 percentage points relative to WT (WT: 53.9 %, L858R: 65.1 %, TMLR: 72.0 %).

In contrast, AMBER apo simulations showed relatively uniform salt bridge occupancy in the receiver chain across variants (WT: 93.8 %, L858R: 92.6 %, TMLR: 94.1 %). However, activator chain occupancies were generally lower than in CHARMM and showed more variation between mutants. Notably, TMLR exhibited the highest occupancy in the apo activator chain, more than 40 percentage points above WT (WT: 15.0 %, L858R: 41.6 %, TMLR: 59.8 %).

In CHARMM holo simulations, salt bridge occupancy in the receiver chain was slightly higher for L858R than in WT (WT: 72.6 %, L858R: 76.7 %) but was markedly reduced for TMLR (44.4 %). Activator chain occupancies were similar across all variants (WT: 66.8 %, L858R: 67.7 %, TMLR 67.9 %).

In AMBER holo simulations, both L858R and TMLR exhibited lower salt bridge occupancy in the receiver chain compared to WT, with drops of more than 30 percentage points (WT: 92.0 %, L858R: 60.4 %, TMLR: 57.0 %). In contrast, occupancy in the activator chain increased substantially for both mutants compared to WT, especially for L858R (WT: 11.4 %, L858R: 57.6 %, TMLR: 27.6 %).

These simulations revealed several key trends. In all CHARMM simulation conditions, L858R consistently exhibited higher salt bridge occupancy than WT, suggesting stabilization of the active EGFR conformation. In AMBER, this increase occurred only in the activator chain, not in the receiver chain. The difference in salt bridge occupancy

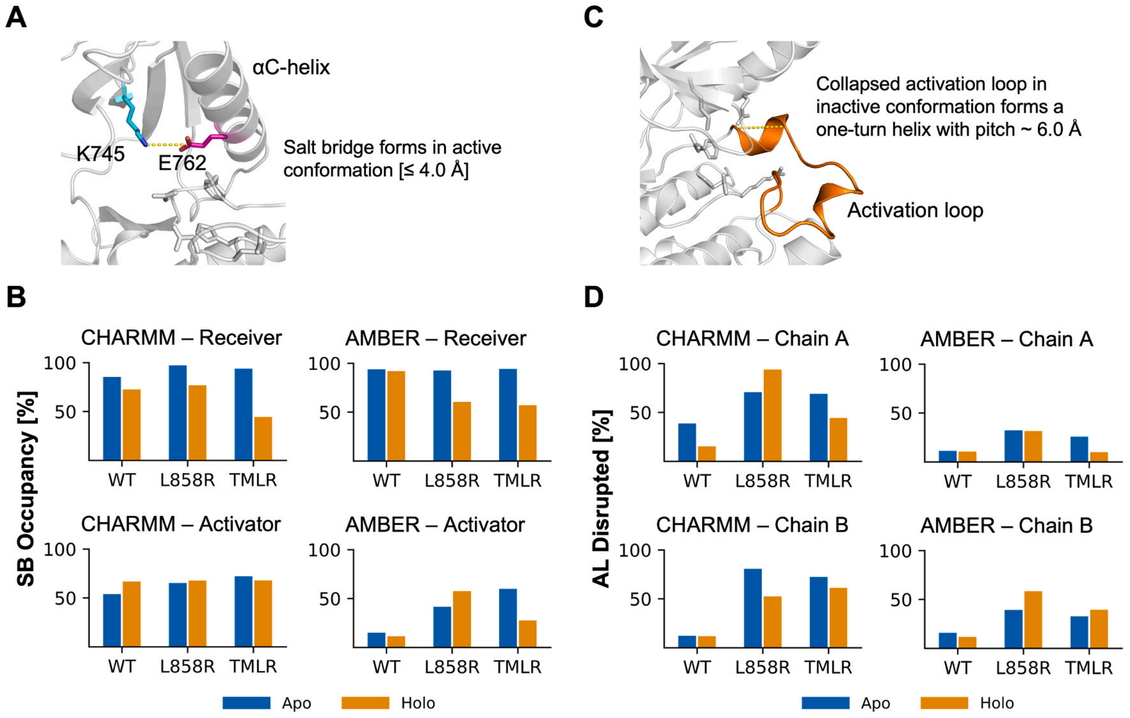

Fig. 2. Benchmarking the CHARMM and AMBER force fields for reproducing known EGFR dynamics. (A) In the active conformation, a salt bridge forms between residues K745 and E762. (B) Salt bridge occupancy using a cutoff of 4.0 Å in simulations of the asymmetric dimer. Values are shown for different force fields, chains, and the presence or absence of ATP. Note that data are presented only for the asymmetric dimer, as the K745 – E762 salt bridge did not form in simulations of the symmetric dimer. (C) In the Src-like inactive conformation, the activation loop is collapsed, forming a short, one-turn helix with a pitch of approximately 6.0 Å. (D) Disruption of the inactive activation loop conformation. The loop was considered disrupted if the helix pitch exceeded 7.0 Å. The percentage of simulation time during which the loop was disrupted is shown for different force fields, chains, and the presence or absence of ATP. Note that data are presented only for the symmetric dimer, as the one-turn helix was not observed in simulations of the asymmetric dimer. Abbreviations: SB = salt bridge, AL = activation loop.

between WT and mutant activator chains was larger in AMBER simulations than CHARMM, largely because WT showed almost no salt bridge formation in the AMBER activator chain. In both force fields, ATP binding reduced receiver chain salt bridge occupancy, likely because ATP's phosphate displaced the E762 carboxylate, causing K745 to interact with ATP instead. As a result, salt bridge occupancy in the holo receiver chain may not reliably indicate stabilization of the active conformation.

3.3. CHARMM vs. AMBER: simulating the symmetric dimer

An alternate mechanism for EGFR overactivation involves destabilization of the inactive state [23,25]. In this model, mutations that reduce compatibility with the inactive state shift the conformational equilibrium toward the active state, potentially resulting in gain-of-function effects. The Src-like inactive conformation features a short, one-turn helix at the start of the activation loop, just after the DFG motif (Fig. 2c). Consistent with previous findings, our symmetric dimer simulations showed more frequent disruption in mutants compared to WT. To quantify this effect, helix disruption in the activation loop was measured as a proxy for inactive state destabilization.

In CHARMM apo simulations of the symmetric dimer, activation loop disruption occurred in 38.7 % and 12.1 % of the simulation time in chains A and B for WT, respectively. In contrast, L858R exhibited substantially higher disruption: 70.6 % of the simulation time in chain A (30 percentage points higher than WT) and 80.6 % of the time in chain B (nearly 70 percentage points higher; Fig. 2d). TMLR showed a similar pattern, with disruption in 69.0 % and 72.3 % of the time in chains A and B, respectively, under CHARMM apo conditions.

AMBER apo simulations also demonstrated increased activation loop disruption in mutants compared to WT, though the effect was less pronounced than in CHARMM. In WT, disruption occurred in 11.2 % and 15.8 % of the simulation time in chains A and B, respectively. L858R increased disruption by over 20 percentage points, with 32.1 % in chain A and 39.2 % in chain B. TMLR exhibited a more moderate increase, with disruption observed 25.8 % and 32.7 % of the time in chains A and B, respectively.

In CHARMM holo simulations, activation loop disruption increased sharply for L858R and TMLR compared to WT. WT exhibited disruption in just 15.3 % and 11.8 % of the time in chains A and B, whereas L858R rose to 93.8 % and 52.5 %, respectively. TMLR also displayed increased disruption, at 44.3 % and 61.1 % in chains A and B, respectively.

In AMBER holo simulations, activation loop disruption in WT occurred 10.5 % and 11.6 % of the time in chains A and B, respectively. L858R increased disruption in both chains (31.6 % and 58.4 % of the time), TMLR showed no increase in chain A (9.9 %) but a substantial increase in chain B (39.4 %).

Overall, both CHARMM and AMBER simulations demonstrated that L858R and TMLR disrupt the inactive activation loop conformation more than WT. The effect was more pronounced in CHARMM, where the absolute increase in disruption was greater. While full transition to an extended activation loop conformation was not observed, the disruption of the activation loop helix suggests that L858R and TMLR destabilize the inactive state.

3.4. Evaluation of the benchmarking study

We then evaluated which protocol to use for simulating additional variants. While both force fields produced results that generally aligned with existing findings for WT and mutants, we opted to continue using only the CHARMM force field for two main reasons. First, CHARMM more consistently captured the expected increase in K745 – E762 salt bridge stability of L858R relative to WT in asymmetric dimer simulations (Fig. 2b). While AMBER showed a more pronounced increase in salt bridge occupancy in the activator chain for L858R relative to WT compared to CHARMM, it showed no increase in occupancy in the receiver chain. Second, CHARMM better captured the destabilization of the inactive state by the cancer mutants (Fig. 2d). In CHARMM simulations, L858R and TMLR caused a more pronounced disruption of the inactive activation loop conformation relative to WT, compared to AMBER simulations. We therefore concluded that using the CHARMM force field alone is sufficient to capture mutational overactivation.

We then applied this MD protocol to study the rare mutations S768I, S768N, and D761N. Each mutant was simulated in asymmetric and symmetric dimeric forms under apo and holo conditions with the CHARMM force field for 500 ns per system, totaling 2 μs per mutant (Table S2). Overall structural stability was observed across all systems based on RMSD analysis (Figure S3).

3.5. S768I exhibits increased hydrophobic packing between αC-helix and activation loop

The oncogenic mutation S768I has been reported to stabilize the αC-helix and enhance K745 – E762 salt bridge formation compared to the wild-type. This stabilization has been attributed to increased hydrophobic packing introduced by the mutation. To assess whether our simulations reproduced these findings, we analyzed salt bridge formation, secondary structure stability, and the number of hydrophobic contacts formed by residue 768. Additionally, we investigated whether S768I disrupts the inactive conformation.

As expected, apo simulations of the asymmetric dimer confirmed that the K745 – E762 salt bridge is more stable in S768I than in WT (Fig. 3a): the salt bridge forms 96.6 % of the time in the receiver chain of

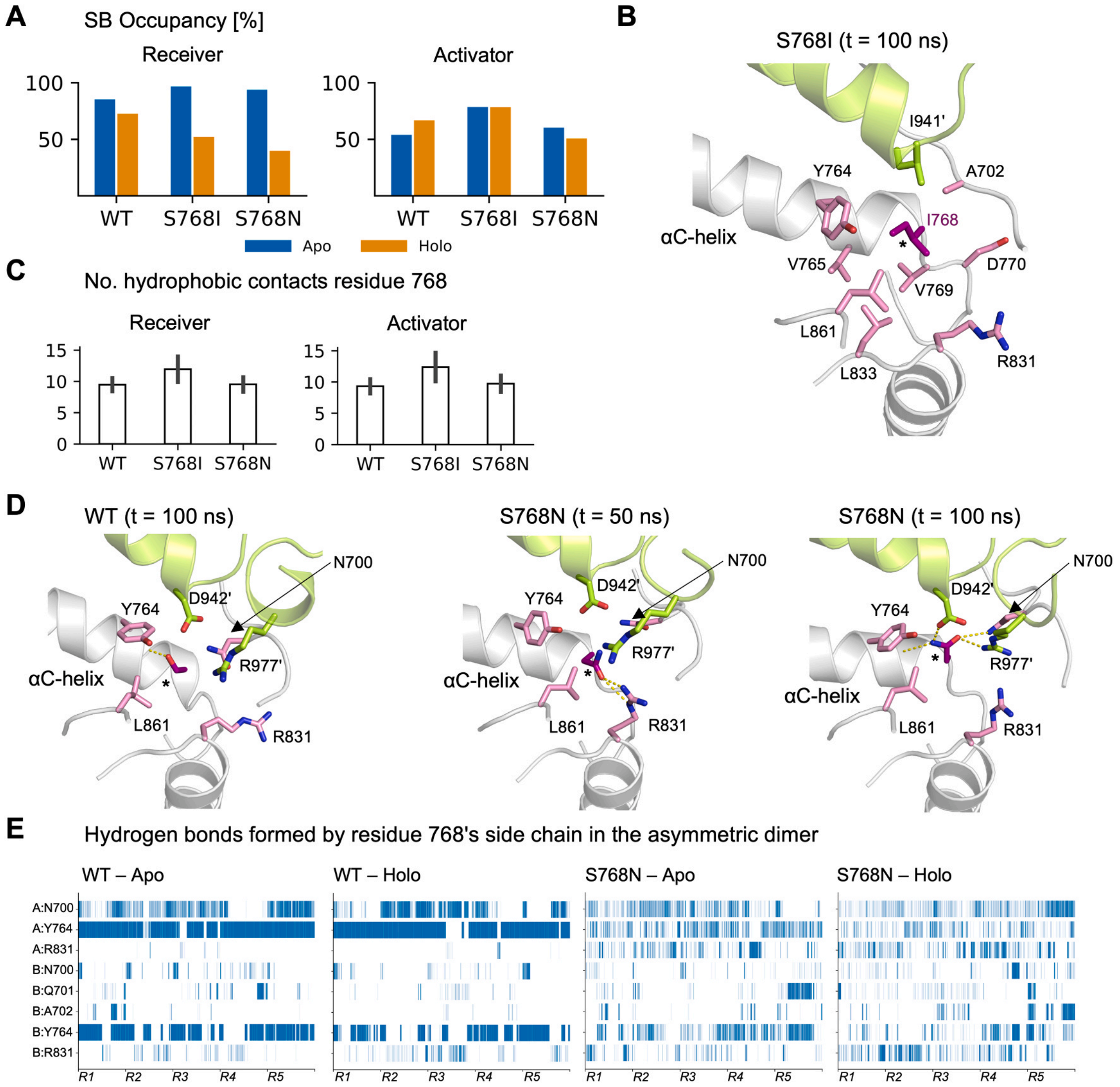

Fig. 3. Allosteric regulation in the mutant pair S768I and S768N. (A) Comparison of salt bridge occupancy in the asymmetric dimer among WT, S768I, and S768N, analogous to Fig. 2b. (B) Snapshot of the S768I mutant in the asymmetric dimer conformation after 100 ns of simulation time. The mutant residue I768 and surrounding residues form a hydrophobic network. The receiver and activator chains are highlighted in light gray and green, respectively. I768 is highlighted in purple and labeled with an asterisk. Other residues of the receiver chain are shown in pink stick representation, while residues of the activator chain are depicted in green stick representation. (C) Average number of hydrophobic contacts between residue S/I/N768 and its neighboring residues in the asymmetric dimer, calculated across both Apo and Holo systems. Error bars show standard deviation. (D) Snapshots of WT and the S768N mutant at different simulation times. Hydrogen bonds involving the sidechain of residue 768 are shown as yellow dashed lines. The receiver and activator chains are highlighted in light gray and green, respectively. Residue 768 is highlighted in purple and labeled with an asterisk. Other residues of the receiver chain are shown in pink stick representation, while residues of the activator chain are depicted in green stick representation. (E) Hydrogen bond existence map illustrating interactions between the sidechain of residue 768 and its surrounding environment over time. Each residue is labeled by its chain: A = receiver chain, B = activator chain. Only the most frequently observed hydrogen bonds are depicted. Data from all replicas are combined for each system. Abbreviations: SB = salt bridge, R = replica.

S768I (WT: 85.4 %, for comparison: L858R: 97.1 %) and 78.4 % of the time in the activator chain, which is more than 20 percentage points higher than WT (WT: 53.9 %, L858R: 65.1 %). In the holo simulations of the asymmetric dimer, S768I exhibited decreased salt bridge formation (51.9 %) relative to WT in the receiver chain (WT: 72.6 %, L858R: 76.7 %), but increased formation (78.3 %) in the activator chain (WT: 66.8 %, L858R: 67.7 %). To determine whether the mutated residue directly interacts with the salt bridge residues, we measured its proximity to key catalytic sites. In all simulations, the sidechain heavy atoms of both WT and mutant residue 768 remained beyond 7 Å from the side chains of K745 and E762, 10 Å from the sidechain of the catalytic aspartate D855 of the DFG motif, and 13 Å from any ATP heavy atom. Therefore, residue S768 does not directly interact with ATP or catalytically relevant residues, suggesting an allosteric mechanism for the increase in salt bridge formation.

To investigate the reported stabilization of the active conformation of the αC-helix, we assessed its secondary structure stability using the DSSP method. Consistent with previous findings, S768I exhibited greater αC-helix stability in the asymmetric dimer compared to WT, with a higher average number of residues assigned as 'helical' in both apo and holo simulations. In the apo state, this increase was observed in both the receiver (S768I: 15.4 ± 1.1, WT: 15.0 ± 1.2) and activator (S768I: 15.4 ± 1.1, WT: 15.1 ± 1.4) chains. A similar trend was seen in holo simulations, with S768I maintaining a higher number of helical residues in both the receiver (S768I: 15.7 ± 0.8, WT: 14.6 ± 1.4) and activator (S768I: 14.9 ± 1.5, WT: 14.7 ± 1.5) chains.

To quantify the reported increase in hydrophobic packing, we measured hydrophobic contacts between residue 768 and its neighboring residues (Fig. 3b,c). Supporting previous claims, S768I exhibited approximately 30 % more hydrophobic interactions than WT. This increase was observed in all conditions: apo receiver chain (WT: 9.4 ± 0.9, S768I: 11.8 ± 2.0), apo activator chain (WT: 9.4 ± 1.1, S768I: 12.3 ± 2.3), holo receiver chain (WT: 9.4 ± 1.0, S768I: 12.1 ± 2.0), and holo activator chain (WT: 9.2 ± 1.0, S768I: 12.5 ± 2.3).

We also analyzed the disruption of the short one-turn helix in the collapsed activation loop in simulations of the inactive, symmetric dimer. Compared to WT, S768I exhibited reduced activation loop disruption in apo chain A (WT: 38.7 %, S768I: 27.8 %) but increased disruption in apo chain B (WT: 12.1 %, S768I: 38.4 %), holo chain A (WT: 15.3 %, S768I: 16.5 %), and holo chain B (WT: 11.8 %, S768I: 27.6 %). However, even in systems where S768I increased disruption of the inactive state, the effect was less pronounced than in L858R or TMLR (Fig. 2d and Table S3), suggesting that S768I does not strongly destabilize the inactive state.

In summary, our simulations of the asymmetric dimer showed that S768I increases salt bridge formation under apo conditions, enhances αC-helix stability, and strengthens hydrophobic packing. Notably, the increase in salt bridge formation was comparable to or greater than that observed for the strongly oncogenic L858R under all conditions, except in the receiver chain in holo simulations, where – as mentioned in Section 3.2 – salt bridge stability may not be an indicative measure of EGFR overactivation. The increase in hydrophobic interactions between the mutated residue 768 and hydrophobic residues from both the αC-helix and activation loop (Fig. 3b,c) likely contributes to the observed stabilization of the αC-helix. Given that E762, one of the two residues involved in the catalytic salt bridge, is part of the αC-helix, this stabilization may play a role in reinforcing the salt bridge. Since S768I did not induce as strong a disruption of the inactive state as L858R and TMLR, we hypothesize that its oncogenic effects primarily stem from stabilizing the active state rather than destabilizing the inactive conformation.

3.6. S768N increases local disorder through formation of a dynamic hydrogen bonding network

To investigate the structural basis for the presumed non-activating behavior of the S768N mutant, we performed the same analyses as for the oncogenic S768I mutant. As expected, S768N exhibited reduced salt bridge formation and weaker hydrophobic packing compared to S768I (Fig. 3a,c) in the asymmetric dimer. Additionally, αC-helix stability in S768N was either lower or comparable to WT. In the apo state, this reduction was observed in both the receiver (S768N: 14.2 ± 1.2, WT: 15.0 ± 1.2) and activator (S768N: 14.5 ± 1.5, WT: 15.1 ± 1.4) chains. A similar trend was seen in holo simulations, where S768N maintained comparable or reduced numbers of helical residues in both the receiver (S768N: 14.7 ± 1.5, WT: 14.6 ± 1.4) and activator (S768N: 14.3 ± 2.0, WT: 14.7 ± 1.5) chains.

We also analyzed the disruption of the collapsed activation loop in the symmetric dimer. Compared to WT and S768I, S768N exhibited increased activation loop disruption. However, this effect was less pronounced than in L858R or TMLR (Table S3). These findings suggest that S768N is unlikely to confer a gain of function, supporting its classification as a neutral mutation. To further explore why the structural changes caused by S768N were likely insufficient to drive overactivation, we investigated their impacts on the local hydrogen bonding network.

We hypothesized that the asparagine substitution in S768N might alter hydrogen bonding patterns, thereby affecting the stability of the active conformation. To test this, we analyzed hydrogen bonding interactions involving the serine side chain in WT and the asparagine side chain in S768N (Fig. 3d). Interestingly, while S768N is theoretically capable of forming more hydrogen bonds – at times forming up to five simultaneously in our simulations – the average number of hydrogen bonds observed across simulation snapshots was equal to or lower than in WT. In apo simulations of the asymmetric dimer, the WT serine side chain formed an average of 1.4 ± 0.6 and 0.9 ± 0.7 hydrogen bonds in the receiver chain and the activator chains, respectively. In contrast, the S768N side chain formed 0.9 ± 0.7 and 0.8 ± 0.9 hydrogen bonds in the receiver and activator chains, respectively. Similar trends were observed in holo simulations, where WT formed 1.3 ± 0.5 and 0.8 ± 0.6 hydrogen bonds, while S768N formed 0.8 ± 0.7 and 0.9 ± 0.9 hydrogen bonds in the receiver and activator chains, respectively.

Next, we examined the hydrogen bonding partners of residue 768 in our asymmetric dimer simulations (Fig. 3e). In WT, hydrogen bonds were primarily formed with the backbone carbonyl oxygen of the αC-helix residue Y764 and, less frequently, with the side chain of N700 in the N-terminal tail. In contrast, the side chain of S768N exhibited greater flexibility, frequently switching hydrogen bonding partners between N700, Y764, and R831 (located in the αE-helix of the C-lobe), with occasional interactions with Q701 and A702. We propose that this increased flexibility, which resulted in an overall reduction in hydrogen bond stability due to numerous short-lived interactions, contributes to greater disorder in the αC-helix and may explain the presumed non-activating behavior of S768N. Interestingly, in the inactive, symmetric dimer, S768N formed slightly more hydrogen bonds than WT (Table S4), potentially suggesting a modest stabilizing effect on the inactive state.

3.7. D761N forms a new hydrogen bonding pattern between the αC-helix and activation loop

We also simulated the oncogenic exon 19 mutation D761N, located near the center of the αC-helix. When measuring salt bridge occupancy in the apo asymmetric dimer, we found that D761N exhibited the highest occupancy among all simulated mutants in the receiver chain, increasing by 12 percentage points compared to WT (from 85.4 % to 97.5 %, Fig. 4a). In contrast, salt bridge occupancy decreased in the activator chain (WT: 53.9 %, D761N: 49.3 %). This suggests that D761N primarily stabilizes the active conformation in the receiver chain but not in the activator chain. Additionally, D761N did not increase activation loop disruption relative to WT in the inactive, symmetric dimer (Table S3). Therefore, similar to S768I, our simulations suggest that D761N primarily stabilizes the active state rather than destabilizing the inactive state.

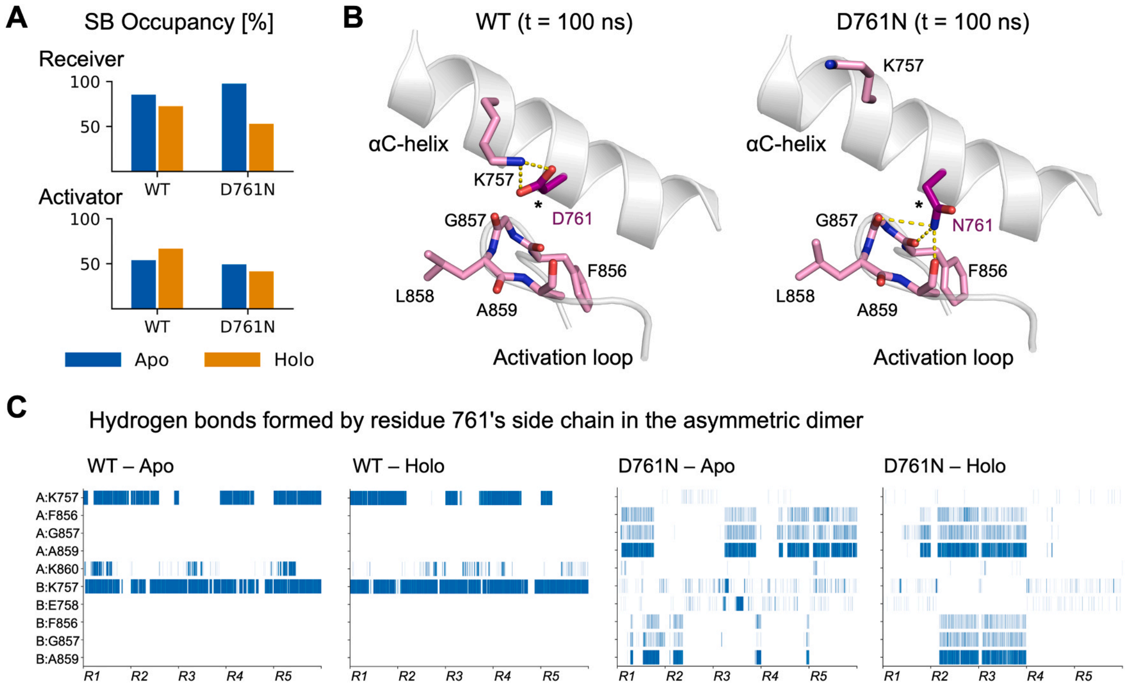

Fig. 4. The D761N mutation forms a new hydrogen bonding pattern between the αC-helix and the activation loop. (A) Comparison of salt bridge occupancy in the asymmetric dimer among WT and D761N, analogous to Fig. 2b. (B) Snapshots of WT and the D761N mutant after 100 ns of simulation time each. Hydrogen bonds involving the sidechain of residue 761 are shown as yellow dashed lines. The snapshots display the receiver chain, with residue 761 highlighted in purple and marked with an asterisk. For residues 856–859, the backbone atoms are also shown. (C) Hydrogen bond existence map illustrating interactions between the sidechain of residue 761 and its surrounding environment over time. Each residue is labeled by its chain: A = receiver chain, B = activator chain. Only the most frequently observed hydrogen bonds are depicted. Data from all replicas are combined for each system. Abbreviations: SB = salt bridge, R = replica.

To further explore the structural effects of D761N, we examined the local hydrogen bonding network around the mutant site (Fig. 4b). Interestingly, D761N formed a stable alternative hydrogen bonding network distinct from that of WT. In WT, the aspartate side chain of D761 primarily formed a salt bridge with the more N-terminal lysine K757. In contrast, the mutated asparagine side chain in the D761N mutant frequently engaged in hydrogen bonds with the backbones of residues F856, G857, and A859 (Fig. 4c). Notably, F856 and G857 belong to the DFG motif, and all three residues are part of the activation loop. In the apo state, these hydrogens bonds formed more frequently in the receiver chain than in the activator chain, aligning with the high salt bridge stability observed for the apo receiver chain. Conversely, under holo conditions, the hydrogen bond formation was more balanced between the receiver and activator chains, which also corresponded to the similar salt bridge occupancy between the holo receiver and activator chains (Fig. 4a). These findings suggest that D761N stabilizes a novel hydrogen bonding pattern between the αC-helix and the activation loop, potentially promoting the active conformation allosterically and contributing to oncogenicity.

4. Discussion

4.1. A novel protocol to study EGFR overactivation

Long-timescale unbiased MD simulations have been widely employed to study EGFR conformational transitions, with some studies extending into the hundreds of microseconds of simulation time [11,12]. Others have used enhanced sampling methods to explore a broader conformational space [13,25]. Here, we presented a protocol that utilizes sets of 500 ns unbiased simulations to compare the dynamics of wild-type EGFR and its mutants. This timescale is sufficient to observe disruptions in the active EGFR state [11]. Although the Src-like inactive state is relatively stable – having been simulated for up to 100 μs in previous studies – our analysis of activation loop stability in the inactive, symmetric dimer captured local disruptions well within our 500 ns simulation time frame. To ensure reproducibility in system preparation and simulation setup, we used the well-established CHARMM-GUI web interface (see Methods). This approach standardizes the simulation workflow, particularly for extending studies to additional EGFR variants. Furthermore, our analysis steps are easily repeatable and can serve as a blueprint for studying other EGFR mutations or even other kinase family members.

By simulating both the active, asymmetric dimer and the inactive, symmetric dimer, our protocol predicts whether a mutation primarily affects the active state, the inactive state, or both. This distinction has practical implications for drug design, as different classes of tyrosine kinase inhibitors (TKIs) preferentially target specific EGFR conformations [52]. Among the non-covalent binders, Type I TKIs bind to the active kinase conformation, whereas Type I ½ and Type II inhibitors preferentially bind to the Src-like (DFG-in) inactive and DFG-out inactive conformations, respectively. Type III inhibitors are allosteric compounds that bind adjacent to the ATP-binding site, while Type IV inhibitors bind in more distal allosteric regions. Recent developments include Type V bivalent inhibitors, which occupy both the ATP and allosteric pockets [53], and novel ATP-site binders that induce conformational changes in the αC-helix [54]. The latter approach may be particularly promising for variants such as S768I and D761N, for which our simulations indicated that the αC-helix plays an integral role in their mechanism of overactivation. Notably, both variants have been associated with resistance or reduced sensitivity to TKI I and I ½ inhibitors such as gefitinib and erlotinib [31,55]. By identifying which conformational state is preferentially stabilized by a given mutation, and elucidating its mechanism of overactivation, our protocol may help inform the selection of inhibitor classes that are most likely to be effective for individual variants.

4.2. Applicability to further variants

We aimed to establish criteria to determine whether a mutation is likely oncogenic based on our protocol. Our results suggest that CHARMM apo simulations alone are sufficient to distinguish between oncogenic and neutral mutants. Across these simulations, we observed that all oncogenic mutations examined in this study (L858R, TMLR, S768I, and D761N) increased K745 – E762 salt bridge occupancy by at least 10 percentage points in at least one chain of the apo asymmetric dimer, relative to WT, which exhibited occupancies of 85.4 % and 53.9 % in the receiver and activator chains, respectively. Notably, L858R and S768I met this threshold in both chains. In addition, TMLR and L858R were the only oncogenic mutants that consistently exhibited high disruption of the inactive state. Under apo conditions, both mutations disrupted the inactive conformation in more than 60 % of the simulation time for both chains – a threshold that no other mutant exceeded in apo simulations. Based on these observations, a mutation is likely oncogenic if it meets at least one of the following three criteria in apo simulations: (i) salt bridge occupancy of ~95 % or higher in the receiver chain of the asymmetric dimer, (ii) salt bridge occupancy of ~64 % or higher in the activator chain of the asymmetric dimer, (iii) disruption of the inactive state in at least 60 % of the simulation time for both chains in the symmetric dimer. We suspect that the likelihood of oncogenic hyperactivation increases when multiple criteria are met. Additionally, if ambiguity remains, holo simulations may provide further insights.

5. Conclusion

The EGFR kinase domain exhibits a vast mutational landscape, with nearly 1000 recorded somatic mutations cataloged in COSMIC, including over 500 missense mutations. Despite this diversity, only a small fraction of these mutants has been biochemically characterized, and even fewer have been studied at the structural level. Our MD protocol successfully captured the differences between wild-type EGFR and the oncogenic and neutral mutations studied here. For the frequent oncogenic mutations L858R and T790M/L858R, our simulations demonstrated both stabilization of the active state and disruption of the inactive state, consistent with their known oncogenic mechanisms. In contrast, the rare oncogenic mutations S768I and D761N stabilized the active conformation, with our simulations suggesting distinct allosteric mechanisms as the underlying cause – either through increased hydrophobic packing around the αC-helix (S768I) or the formation of a new hydrogen bonding network between the αC-helix and activation loop (D761N). Meanwhile, the neutral mutation S768N failed to stabilize the active conformation, likely due to an unstable and overly flexible hydrogen bonding network introduced by the mutation. Importantly, our study demonstrates that even relatively short 500 ns simulations – which can typically be completed within two days on modern computational hardware – are sufficient to capture key mutational effects on EGFR overactivation. These results highlight the potential of MD simulations for rapidly screening EGFR mutations and gaining insights into their structural and functional consequences.

CRediT authorship contribution statement

Julian Behn: Writing – review & editing, Writing – original draft, Visualization, Validation, Software, Methodology, Investigation, Data curation. **Jiancheng Hu:** Writing – review & editing, Validation, Supervision, Conceptualization. **R. N. V. Krishna Deepak:** Writing – review & editing, Supervision, Project administration, Methodology, Investigation, Conceptualization. **Hao Fan:** Writing – review & editing, Supervision, Resources, Project administration, Methodology, Investigation, Conceptualization.

Declaration of Competing Interest

The authors declare that they have no known competing financial interests or personal relationships that could have appeared to influence the work reported in this paper.

Acknowledgements

The computational work for this article was partially performed on resources of the National Supercomputing Centre (NSCC), Singapore (https://www.nscc.sg). JB is supported by the Singapore International Graduate Award (SINGA), A*STAR, Singapore. HF is supported by funding from Bioinformatics Institute, A*STAR, Singapore.

Appendix A. Supporting information

Supplementary data associated with this article can be found in the online version at doi:10.1016/j.csbj.2025.07.046.

References

[1] Yoshizawa T, Uchibori K, Araki M, Matsumoto S, Ma B, Kanada R, et al. Microsecond-timescale MD simulation of EGFR minor mutation predicts the structural flexibility of EGFR kinase core that reflects EGFR inhibitor sensitivity. NPJ Precis Oncol 2021;5:32.

[2] Hsu WH, Yang JC, Mok TS, Loong HH. Overview of current systemic management of EGFR-mutant NSCLC. Ann Oncol 2018;29:i3–9.

[3] Huang L, Jiang S, Shi Y. Tyrosine kinase inhibitors for solid tumors in the past 20 years (2001-2020). J Hematol Oncol 2020;13:143.

[4] Zhang T, Wan B, Zhao Y, Li C, Liu H, Lv T, et al. Treatment of uncommon EGFR mutations in non-small cell lung cancer: new evidence and treatment. Transl Lung Cancer Res 2019;8:302–16.

[5] Stamos J, Sliwkowski MX, Eigenbrot C. Structure of the epidermal growth factor receptor kinase domain alone and in complex with a 4-anilinoquinazoline inhibitor. J Biol Chem 2002;277:46265–72.

[6] Kovacs E, Zorn JA, Huang Y, Barros T, Kuriyan J. A structural perspective on the regulation of the epidermal growth factor receptor. Annu Rev Biochem 2015;84:739–64.

[7] Huse M, Kuriyan J. The conformational plasticity of protein kinases. Cell 2002;109:275–82.

[8] Modi V, Dunbrack Jr RL. Defining a new nomenclature for the structures of active and inactive kinases. Proc Natl Acad Sci USA 2019;116:6818–27.

[9] Moritsugu K, Nishino T, Kidera A. Inter-lobe motions allosterically regulate the structure and function of EGFR kinase. J Mol Biol 2020;432:4561–75.

[10] Honegger AM, Dull TJ, Felder S, Van Obberghen E, Bellot F, Szapary D, et al. Point mutation at the ATP binding site of EGF receptor abolishes protein-tyrosine kinase activity and alters cellular routing. Cell 1987;51:199–209.

[11] Shan Y, Eastwood MP, Zhang X, Kim ET, Arkhipov A, Dror RO, et al. Oncogenic mutations counteract intrinsic disorder in the EGFR kinase and promote receptor dimerization. Cell 2012;149:860–70.

[12] Shan Y, Arkhipov A, Kim ET, Pan AC, Shaw DE. Transitions to catalytically inactive conformations in EGFR kinase. Proc Natl Acad Sci USA 2013;110:7270–5.

[13] Li Y, Li X, Ma W, Dong Z. Conformational transition pathways of epidermal growth factor receptor kinase domain from multiple molecular dynamics simulations and Bayesian clustering. J Chem Theory Comput 2014;10:3503–11.

[14] Galdadas I, Carlino L, Ward RA, Hughes SJ, Haider S, Gervasio FL. Structural basis of the effect of activating mutations on the EGF receptor. Elife 2021;10.

[15] Zhang X, Gureasko J, Shen K, Cole PA, Kuriyan J. An allosteric mechanism for activation of the kinase domain of epidermal growth factor receptor. Cell 2006;125:1137–49.

[16] Jura N, Endres NF, Engel K, Deindl S, Das R, Lamers MH, et al. Mechanism for activation of the EGF receptor catalytic domain by the juxtamembrane segment. Cell 2009;137:1293–307.

[17] Ruan Z, Kannan N. Mechanistic insights into R776H mediated activation of epidermal growth factor receptor kinase. Biochemistry 2015;54:4216–25.

[18] Ding X, Liu X, Song X, Yao J. Chemotherapy drug response to the L858R-induced conformational change of EGFR activation loop in lung cancer. Mol Inf 2016;35:529–37.

[19] Harrison PT, Vyse S, Huang PH. Rare epidermal growth factor receptor (EGFR) mutations in non-small cell lung cancer. Semin Cancer Biol 2020;61:167–79.

[20] Robichaux JP, Le X, Vijayan RSK, Hicks JK, Heeke S, Elamin YY, et al. Structure-based classification predicts drug response in EGFR-mutant NSCLC. Nature 2021;597:732–7.

[21] Laudadio E, Piccirilli F, Vondracek H, Mobbili G, Semrau MS, Storici P, et al. Probing conformational dynamics of EGFR mutants via SEIRA spectroscopy: potential implications for tyrosine kinase inhibitor design. Phys Chem Chem Phys 2024;26:22853–7.

[22] Gazdar AF. Activating and resistance mutations of EGFR in non-small-cell lung cancer: role in clinical response to EGFR tyrosine kinase inhibitors. Oncogene 2009;28(1):S24–31.

[23] Yun CH, Boggon TJ, Li Y, Woo MS, Greulich H, Meyerson M, et al. Structures of lung cancer-derived EGFR mutants and inhibitor complexes: mechanism of activation and insights into differential inhibitor sensitivity. Cancer Cell 2007;11:217–27.

[24] Wan S, Coveney PV. Molecular dynamics simulation reveals structural and thermodynamic features of kinase activation by cancer mutations within the epidermal growth factor receptor. J Comput Chem 2011;32:2843–52.

[25] Sutto L, Gervasio FL. Effects of oncogenic mutations on the conformational free-energy landscape of EGFR kinase. Proc Natl Acad Sci USA 2013;110:10616–21.

[26] Yun CH, Mengwasser KE, Toms AV, Woo MS, Greulich H, Wong KK, et al. The T790M mutation in EGFR kinase causes drug resistance by increasing the affinity for ATP. Proc Natl Acad Sci USA 2008;105:2070–5.

[27] Banno E, Togashi Y, Nakamura Y, Chiba M, Kobayashi Y, Hayashi H, et al. Sensitivities to various epidermal growth factor receptor-tyrosine kinase inhibitors of uncommon epidermal growth factor receptor mutations L861Q and S768I: what is the optimal epidermal growth factor receptor-tyrosine kinase inhibitor? Cancer Sci 2016;107:1134–40.

[28] Leventakos K, Kipp BR, Rumilla KM, Winters JL, Yi ES, Mansfield AS. S768I mutation in EGFR in patients with lung cancer. J Thorac Oncol 2016;11:1798–801.

[29] Harada T, Lopez-Chavez A, Xi L, Raffeld M, Wang Y, Giaccone G. Characterization of epidermal growth factor receptor mutations in non-small-cell lung cancer patients of African-American ancestry. Oncogene 2011;30:1744–52.

[30] Ng PK, Li J, Jeong KJ, Shao S, Chen H, Tsang YH, et al. Systematic functional annotation of somatic mutations in cancer. Cancer Cell 2018;33:450–62. e10.

[31] Kancha RK, von Bubnoff N, Peschel C, Duyster J. Functional analysis of epidermal growth factor receptor (EGFR) mutations and potential implications for EGFR targeted therapy. Clin Cancer Res 2009;15:460–7.

[32] Ma L, Li H, Wang D, Hu Y, Yu M, Zhang Q, et al. Dynamic cfDNA analysis by NGS in EGFR T790M-Positive advanced NSCLC patients failed to the First-Generation EGFR-TKIs. Front Oncol 2021;11:643199.

[33] Shih AJ, Telesco SE, Choi SH, Lemmon MA, Radhakrishnan R. Molecular dynamics analysis of conserved hydrophobic and hydrophilic bond-interaction networks in ErbB family kinases. Biochem J 2011;436:241–51.

[34] Songtawee N, Bevan DR, Choowongkomon K. Molecular dynamics of the asymmetric dimers of EGFR: simulations on the active and inactive conformations of the kinase domain. J Mol Graph Model 2015;58:16–29.

[35] Park J, McDonald JJ, Petter RC, Houk KN. Molecular dynamics analysis of binding of kinase inhibitors to WT EGFR and the T790M mutant. J Chem Theory Comput 2016;12:2066–78.

[36] Saldana-Rivera L, Bello M, Mendez-Luna D. Structural insight into the binding mechanism of ATP to EGFR and L858R, and T790M and L858R/T790 mutants. J Biomol Struct Dyn 2019;37:4671–84.

[37] Kannan S, Venkatachalam G, Lim HH, Surana U, Verma C. Conformational landscape of the epidermal growth factor receptor kinase reveals a mutant specific allosteric pocket. Chem Sci 2018;9:5212–22.

[38] Ikemura S, Yasuda H, Matsumoto S, Kamada M, Hamamoto J, Masuzawa K, et al. Molecular dynamics simulation-guided drug sensitivity prediction for lung cancer with rare EGFR mutations. Proc Natl Acad Sci USA 2019;116:10025–30.

[39] Tamirat MZ, Koivu M, Elenius K, Johnson MS. Structural characterization of EGFR exon 19 deletion mutation using molecular dynamics simulation. PLoS One 2019;14:e0222814.

[40] Laudadio E, Mobbili G, Sorci L, Galeazzi R, Minnelli C. Mechanistic insight toward EGFR activation induced by ATP: role of mutations and water in ATP binding patterns. J Biomol Struct Dyn 2023;41:6492–501.

[41] Sali A, Blundell TL. Comparative protein modelling by satisfaction of spatial restraints. J Mol Biol 1993;234:779–815.

[42] Shen MY, Sali A. Statistical potential for assessment and prediction of protein structures. Protein Sci 2006;15:2507–24.

[43] Williams CJ, Headd JJ, Moriarty NW, Prisant MG, Videau LL, Deis LN, et al. MolProbity: more and better reference data for improved all-atom structure validation. Protein Sci 2018;27:293–315.

[44] Abraham MJ, Murtola T, Schulz R, Páll S, Smith JC, Hess B, et al. GROMACS: high performance molecular simulations through multi-level parallelism from laptops to supercomputers. SoftwareX 2015;1-2:19–25.

[45] Huang J, Rauscher S, Nawrocki G, Ran T, Feig M, de Groot BL, et al. CHARMM36m: an improved force field for folded and intrinsically disordered proteins. Nat Methods 2017;14:71–3.

[46] Tian C, Kasavajhala K, Belfon KAA, Raguette L, Huang H, Migues AN, et al. ff19SB: Amino-Acid-Specific protein backbone parameters trained against quantum mechanics energy surfaces in solution. J Chem Theory Comput 2020;16:528–52.

[47] Jo S, Kim T, Iyer VG, Im W. CHARMM-GUI: a web-based graphical user interface for CHARMM. J Comput Chem 2008;29:1859–65.

[48] Brooks BR, Brooks 3rd CL, Mackerell Jr AD, Nilsson L, Petrella RJ, Roux B, et al. CHARMM: the biomolecular simulation program. J Comput Chem 2009;30:1545–614.

[49] Lee J, Cheng X, Swails JM, Yeom MS, Eastman PK, Lemkul JA, et al. CHARMM-GUI input generator for NAMD, GROMACS, AMBER, OpenMM, and CHARMM/OpenMM simulations using the CHARMM36 additive force field. J Chem Theory Comput 2016;12:405–13.

[50] Lee J, Hitzenberger M, Rieger M, Kern NR, Zacharias M, Im W. CHARMM-GUI supports the amber force fields. J Chem Phys 2020;153:035103.

[51] McGibbon RT, Beauchamp KA, Harrigan MP, Klein C, Swails JM, Hernandez CX, et al. MDTraj: a modern open library for the analysis of molecular dynamics trajectories. Biophys J 2015;109:1528–32.

[52] Roskoski Jr R. Classification of small molecule protein kinase inhibitors based upon the structures of their drug-enzyme complexes. Pharm Res 2016;103:26–48.

[53] Wittlinger F, Ogboo BC, Shevchenko E, Damghani T, Pham CD, Schaeffner IK, et al. Linking ATP and allosteric sites to achieve superadditive binding with bivalent EGFR kinase inhibitors. Commun Chem 2024;7:38.

[54] Romagnoli E, Laudadio E, Mobbili G, Sorci L, Birarda G, Piccirilli F, et al. FL30: an epidermal growth factor kinase inhibitor overcoming T790M and C797S mutations through unique conformational modulation mechanism. Int J Biol Macromol 2025;319:145453.

[55] Kohsaka S, Nagano M, Ueno T, Suehara Y, Hayashi T, Shimada N, et al. A method of high-throughput functional evaluation of EGFR gene variants of unknown significance in cancer. Sci Transl Med 2017;9.